

Quantitative Evaluation of Flow Computations by Rainbow Schlieren Deflectometry

Anil K. Shenoy,* Ajay K. Agrawal,† Subramanyam R. Gollahalli‡
University of Oklahoma, Norman, Oklahoma 73019

Rainbow schlieren deflectometry, a line-of-sight optical measurement technique, was used to evaluate computations of steady nonreacting and reacting flows in axisymmetric systems. The nonreacting flow was that of an isothermal helium jet discharged vertically in air, and the reacting flow was that of a hydrogen jet diffusion flame. The computed results were processed to obtain a color schlieren image for direct visual comparison with the corresponding experimental color schlieren image. The computed and measured angular deflections of light rays were also compared. In addition, the computed field distributions of scalar flow properties including the refractive index, species concentration, and temperature were compared quantitatively by inverting the experimental schlieren measurements. The results demonstrate the effectiveness of the rainbow schlieren technique in evaluating the physical models used for flow computations.

Nomenclature

$D_{i\text{-mixture}}$	= mass-averaged diffusion coefficient of species i into the mixture, m^2/s
d	= inside diameter of the jet tube, m
F_c	= focal length of the decollimating lens, m
Fr	= Froude number, (u_e^2/gd)
f	= mixture fraction
g	= gravitational acceleration, m/s^2
L	= linear light ray displacement at the filter plane
Le	= Lewis number, $(\alpha/D_{i\text{-mixture}})$
Re	= Reynolds number, $(u_e d/\nu)$
r	= radial coordinate, m
u	= axial velocity, m/s
v	= radial velocity, m/s
Y	= mass fraction
y	= radial coordinate, m
z	= axial coordinate, m
α	= thermal diffusivity, m^2/s
δ	= normalized refractive index difference, $[(\eta - \eta_a)/\eta_a]$
ϵ	= transverse deflection angle of a light ray, rad
η	= refractive index
κ	= Gladstone-Dale constant
ν	= kinematic viscosity, m^2/s
ρ	= density, kg/m^3

Subscripts

a	= ambient
e	= nozzle exit
i	= species

Introduction

IN the past two decades computational fluid dynamics (CFD) has become an important tool for flow predictions and design. CFD calculations involve physical and numerical models; the capability of these models in simulating a phenomenon must be ascertained before the numerical solutions can be accepted.¹ Computational results are usually validated by comparing them with the experimental

data. Nonintrusive techniques such as laser Doppler velocimetry and particle image velocimetry are commonly used to evaluate the computed flowfield. Optical measurement techniques including Rayleigh and Raman scattering, laser-induced fluorescence, and coherent anti-Stokes Raman scattering (CARS)² are employed to validate predictions of scalar flow properties such as temperature and species concentrations. Another important class of optical techniques are schlieren, shadowgraphy, and interferometry used routinely for flow visualization.³ In these line-of-sight techniques, the light rays pass through the test medium to reveal the flow characteristics in an image. The image data are path integrated, and hence, a direct comparison with the local computations is not feasible. A procedure to construct images of schlieren, shadowgraph, and interferogram from the computed flowfield was developed by Yates.^{4,5} The computed image can be compared with the corresponding experimental image, allowing for validation of the physical models. This approach was used with the shadowgraph method to evaluate computations of the temperature field in the convective flow of water in a square cavity.⁶ In spite of their widespread use for qualitative flow visualization, the line-of-sight techniques have played only a minor role in CFD validation because the measurements often lack quantification.

Recently, a quantitative rainbow schlieren deflectometry (RSD) technique utilizing computer processing of data was developed.⁷ The resulting schlieren image displays inhomogeneities of the medium in color, unlike the conventional monochromatic schlieren image, where such nonuniformities are visualized through intensity variations. In addition to enhancing visualization by amplifying subtle differences in the flowfield, the color schlieren image provides quantitative data to reconstruct field distributions of scalar flow properties. Although the present authors have compared the color schlieren results to probe measurements in a heated air jet,⁸ a helium jet,⁹ and a hydrogen diffusion flame,¹⁰ the rainbow schlieren deflectometry is not yet considered as a standard measurement technique.

Results from the rainbow schlieren technique are comparable to computations at three levels. The first is in visual or qualitative comparison of the color schlieren images; in this case the flow computations are used to create a computational color schlieren image. The second is in the comparison of the path-integrated data, e.g., the angular deflections of light rays. The deflection data are inferred from the experimental schlieren image; the angular deflections from the computed flowfield are obtained by tracing light ray paths through the medium. The third is in the comparison of scalar properties such as the refractive index, density, temperature, and species concentrations. The physical property measured with the schlieren apparatus is the refractive index, which is related to other scalar flow properties. The refractive index field is reconstructed from a single experimental schlieren image if the test medium is two dimensional

Received March 4, 1997; revision received May 27, 1998; accepted for publication May 27, 1998. Copyright © 1998 by the American Institute of Aeronautics and Astronautics, Inc. All rights reserved.

*Graduate Research Assistant, School of Aerospace and Mechanical Engineering; currently Project Engineer, Consulting Services, Automated Analysis Corporation, Peoria, IL 61602.

†Assistant Professor, School of Aerospace and Mechanical Engineering, Senior Member AIAA.

‡Lesch Centennial Professor, School of Aerospace and Mechanical Engineering, Associate Fellow AIAA.

or axisymmetric. Alternatively, the CFD results of density, temperature, and species concentrations are converted to the refractive index field. Thus, a quantitative comparison between measurements and predictions is feasible.

In this paper, we describe an application of the RSD technique to evaluate CFD calculations of nonreacting and reacting flows. In both cases the flow was axisymmetric, laminar, and steady. The nonreacting flow was that of an isothermal helium jet discharged vertically in air. The reacting flow was that of a hydrogen gas jet diffusion flame. Calculations assumed fast chemistry and unity Lewis number. Our results demonstrate that the RSD technique provides new insights and quantitative details to validate the CFD calculations. In the following sections we outline the RSD, provide details of the CFD analysis, and discuss results comparing predictions with the measurements.

RSD

We begin this section with a brief outline of the experimental setup used for the RSD technique. Details of the numerical procedure to create a color schlieren image from the flow computations will follow. We also discuss briefly the inverse process of reconstructing the field distributions from the schlieren image.

Experimental Procedure

In the rainbow schlieren apparatus, shown schematically in Fig. 1, the collimated light from a slit aperture is deflected while passing through a test medium with refractive index gradients. A decollimating lens refocuses the deflected ray to form a displaced image of the source at the filter plane. The filter is a transparent film with a rectangular strip of continuous color gradations. The filtered light rays form a color schlieren image on a charge-coupled device (CCD) array, revealing nonuniformities in the test medium. The image is digitized for quantitative analysis. A distinguishing feature of the RSD technique is that the image color is quantified by a single parameter, hue, using the hue-saturation-intensity color model. Thus, the quantification is independent of the other two color parameters: saturation and intensity. This representation eliminates problems of inhomogeneous absorption of light by the test medium and of nonlinearities in recording intensity variations in a monochromatic system. The transmitted hue at the filter is uniquely related to the linear displacement of the light ray at the filter plane. The relationship between the transmitted hue and ray displacement, also called the filter calibration curve, is established a priori in the schlieren apparatus without the test medium. Additional details are given in Refs. 7–9.

Numerical Procedure

The CFD calculations of density, temperature, and/or species concentrations are used to obtain the refractive index field, which provides the angular deflections of light rays by the medium. The deflections are converted to linear displacements at the filter plane and, subsequently, to a hue map according to the filter calibration curve. The hue map is transformed to the red, green, and blue (RGB) color values at pixel locations to create the color schlieren image. A reverse process decodes the color schlieren image to reconstruct the field distributions. The numerical details of these steps follow.

Density and species concentrations are related to the refractive index using the Gladstone–Dale equation¹¹

$$\eta = 1 + \sum_i \kappa_i \rho_i = 1 + \rho \sum_i \kappa_i Y_i \quad (1)$$

The Gladstone–Dale constants of gases in this study are taken from Ref. 5. Next the collimated light ray paths through the computed refractive index field are traced to obtain the transverse angular deflections. The transverse deflection angle of a light ray at a radial location y in an axisymmetric field is given for small deflections as¹²

$$\varepsilon(y) = 2y \int_y^\infty \frac{d\delta}{dr} \cdot \frac{dr}{\sqrt{(r^2 - y^2)}} \quad (2)$$

The integration in Eq. (2) was performed analytically by linearizing the refractive index gradient between discrete grid locations.¹³ After some algebraic manipulation we obtain

$$\varepsilon(y_j) = 2y_j \sum_{k=j}^{nr-1} \frac{S(k) + T(k)}{(r_{k+1} - r_k)} \quad (3)$$

where $y_j = j \Delta r$ is the radial location, Δr is the radial grid spacing, nr is the total number of radial grid points, and

$$S(k) = [R(k) \cdot r_{k+1} - R(k+1) \cdot r_k] \cdot \ln \left[\frac{P(k+1)}{P(k)} \right] \\ T(k) = [R(k+1) - R(k)] \cdot [Q(k+1) - Q(k)] \quad (4)$$

$$R(k) = \frac{d\delta(r_k)}{dr}, \quad Q(k) = [P(k) - r_k]$$

$$P(k) = \left[r_k + \sqrt{(r_k^2 - r_j^2)} \right]$$

The angular light ray deflection is converted by the decollimating lens to a linear light ray displacement at the filter plane given by

$$L(r_j) = F_c \cdot \tan \varepsilon(r_j) \approx F_c \cdot \varepsilon(r_j) \quad (5)$$

The light ray displacement at the filter plane is transformed to hue in the image according to the filter calibration curve $H(y)$ of the schlieren apparatus. Next the grid points used for flow computations are projected onto the image plane to create the color schlieren image. The experimentally obtained image is 640×480 pixels with a spatial resolution of about $94 \mu\text{m}$. The number of pixels in an image exceeds the number of grid points used for flow computations in the present study. We use bilinear interpolation¹⁴ to find hue at a pixel location in the image from hue at the four neighboring grid points. The calculated hue is transformed to the RGB color values to create the schlieren image. Because hue is the only parameter used to characterize the color, we fix the saturation and intensity at a constant value of 1.0.

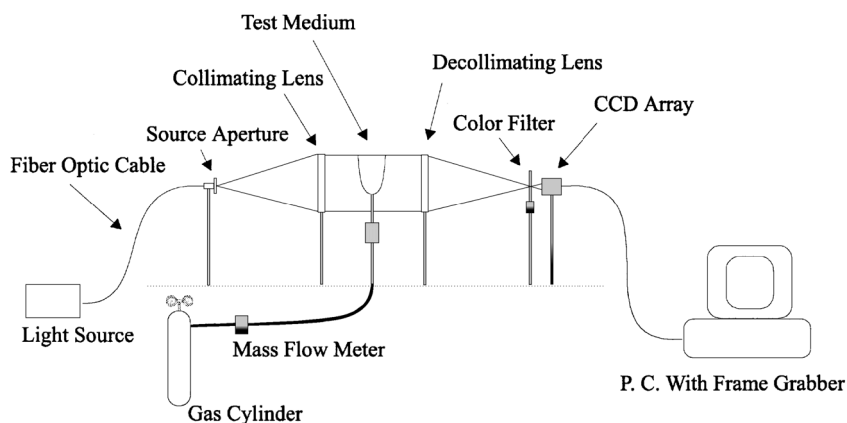


Fig. 1 Schematic of the rainbow schlieren apparatus.

A reverse process provides the angular light ray deflections from the color schlieren image. The experimental data usually contain random fluctuations because of the high-frequency noise, which is removed by filtering using the fast Fourier transform.¹⁴ The refractive index field is found by inverting Eq. (2) using the Abel transformation¹³

$$\delta(r) = -\frac{1}{\pi} \int_r^\infty \varepsilon(y) \cdot \frac{dy}{\sqrt{(y^2 - r^2)}} \quad (6)$$

Equation (6) is expressed in the following discrete form:

$$\delta(r_i) = \sum_{j=i}^{nr} D_{ij} \cdot \varepsilon_j \quad (7)$$

where

$$D_{ij} = J_{ij} \quad \text{if} \quad j = i \\ = J_{ij} + J_{i,j-1} \quad \text{if} \quad j > i \quad (8)$$

$$J_{ij} = -\frac{1}{2\pi} \cdot \ln \left\{ \frac{j+1 + [(j+1)^2 - i^2]^{\frac{1}{2}}}{j + (j^2 - i^2)^{\frac{1}{2}}} \right\} \quad (9)$$

The refractive index thus obtained is related to the scalar flow properties according to Eq. (1).

Flow Computations

The governing equations for a laminar, steady, and axisymmetric flow are expressed in the cylindrical coordinate system as follows:

$$\frac{\partial}{\partial z}(\rho u) + \frac{1}{r} \frac{\partial}{\partial r}(\rho v r) = 0 \quad (10)$$

$$\frac{\partial}{\partial z}(\rho u \phi) + \frac{1}{r} \frac{\partial}{\partial r}(\rho v r \phi) = \frac{\partial}{\partial z} \left(\Gamma^\phi \frac{\partial \phi}{\partial z} \right) + \frac{1}{r} \frac{\partial}{\partial r} \left(\Gamma^\phi r \frac{\partial \phi}{\partial r} \right) + S^\phi \quad (11)$$

Equation (10) is the continuity equation, and Eq. (11) represents a general transport equation, which reduces to the momentum, energy, or species conservation equation, depending on the variable ϕ . The terms Γ^ϕ and S^ϕ in Eq. (11) represent, respectively, the diffusion coefficient and source term of the variable ϕ . The specific details of simulations for the two test cases are described in the next section.

Helium Jet

The computations were done to simulate the experiment with a helium jet discharged vertically into ambient air. The jet tube had an i.d. of 7.2 mm and a wall thickness of 1.0 mm. The Reynolds number and Froude number based on the jet exit conditions were, respectively, 150 and 80. The jet was laminar and weakly buoyant, and the temperature and pressure variations were negligible.¹⁵ In this study, we considered the jet flow to be a binary fluid system by treating air as a single species. In this binary system the species concentrations and, hence, the fluid properties were uniquely related to the helium mass fraction because $Y_{\text{air}} = 1 - Y_{\text{He}}$. Accordingly, we solved for the transport equation of helium mass fraction together with the conservation equations of the mixture mass and momentum. The helium mass fraction equation was obtained by substituting $\phi = f_{\text{He}}$, $\Gamma^\phi = D_{\text{He-mixture}}$, and $S^\phi = 0$ in the generalized transport equation (11). The mixture density was found from the ideal gas law. The kinematic viscosity and helium mass diffusion coefficient $D_{\text{He-mixture}}$ were calculated from Wilke's mixture averaged formula.¹⁶

Hydrogen Diffusion Flame

Computations of the reacting flow introduce complexities of representing the chemical reactions and the energy release associated with them. Also, the physical and transport properties vary with temperature and species concentrations. In this study we assume fast chemistry and unity Lewis number to reduce all of the species concentrations and enthalpy to a single variable for the mixture fraction.¹⁷ Measurements in hydrogen diffusion flames¹⁸ have shown that the major species concentrations and temperature

agree with the thermodynamic equilibrium calculations, especially in the oxidizer side of the flame. The fast-reaction limit is suggested to be adequate for hydrogen flame simulations.¹⁹ Identical results were obtained from computations of a low-speed hydrogen diffusion flame using fast chemistry and finite rate chemistry, when the Lewis number was unity.²⁰ Our representation of fast chemistry using the mixture fraction approach differs from that of other investigators²⁰⁻²² using a global one-step chemical kinetics model. The mixture density, temperature, and species concentrations at chemical equilibrium were found using the Chemkin²³ computer code as functions of the mixture fraction, assuming a constant pressure. The species for equilibrium calculations included H_2 , H_2O , O_2 , N_2 , H , HO_2 , H_2O_2 , O , OH , N , and NO . We solved the transport equation of the mixture fraction together with the conservation equations of the mixture mass and momentum. The mixture fraction follows Eq. (11), with the source term S^ϕ being identically zero. The diffusion coefficient Γ^f , however, requires adequate representation, as discussed next.

The mixture fraction uniquely describes the transport of all species and enthalpy by assuming equal thermal and mass diffusivities. This implies that the Lewis number Le_i for the species i defined as the ratio of the thermal diffusivity α and mass diffusivity $D_{i\text{-mixture}}$ is unity for all species. Recent diffusion flame experiments^{24,25} using hydrogen mixed with heavier inert gases have shown differential diffusion among species and preferential diffusion between heat and mass. For example, the hydrogen-to-carbon mass ratio near the jet centerline was half of that in the fuel (a mixture of H_2 and CO_2) because the hydrogen diffuses more rapidly than CO_2 (Ref. 24). The differential diffusion was most significant on the fuel-rich side of the flame because of the H_2 . Several species, including N_2 , O_2 , CO_2 , CO , and H_2O , did not differentially diffuse to any significant degree. Takagi et al.²⁵ found that the temperature at the flame tip was lower than the adiabatic flame temperature in a diffusion flame of a fuel with 30% H_2 and 70% N_2 . The observed difference was attributed to the preferential diffusion between species and heat. Several theoretical studies have investigated effects of the preferential diffusion and nonunity Lewis number on the flame structure and dynamics.^{20,26-28} In this study, we use pure hydrogen fuel, which minimizes the differential diffusion among species. In this system the major species are N_2 , O_2 , and H_2O , which do not differentially diffuse,²⁴ and H_2 , which is present only in the fuel-rich side of the flame. We predict the flame characteristics using two limiting values of Γ^f in the mixture fraction equation: 1) the mass diffusivity of a representative species and 2) the thermal diffusivity of the mixture. The mass diffusion inside the flame was approximated by diffusion of hydrogen into the mixture, and that outside the flame was represented by diffusion of oxygen into the mixture. Accordingly, the two models developed to simulate the hydrogen diffusion flame are summarized.

Model 1:

$$\Gamma^f = D_{i\text{-mixture}} = \alpha \quad (12)$$

Model 2:

$$\Gamma^f = D_{i\text{-mixture}} = D_{\text{H}_2\text{-mixture}} \quad \text{if} \quad f \geq f_{\text{stoic}} \\ \Gamma^f = D_{i\text{-mixture}} = D_{\text{O}_2\text{-mixture}} \quad \text{if} \quad f < f_{\text{stoic}} \quad (13)$$

The two-zone approach of model 2 is similar to that of Katta et al.^{20,21} to account for the high diffusivity of hydrogen inside the flame. The transport properties, including the momentum diffusivity (or kinematic viscosity), thermal diffusivity, and mass diffusivity, were obtained as functions of the mixture fraction using the Wilke's mixture averaged formula.^{16,29} Figure 2 shows variations of diffusivities, Lewis number, and Schmidt number with the equivalence ratio. Figure 2 reveals that all of the diffusivities reach the peak value in the stoichiometric region. Near the flame, the mass diffusivity was the highest, and the momentum diffusivity was the lowest. The Lewis number was almost unity at fuel-lean conditions. The Lewis number was below unity between equivalence ratios of 1.0 and 7.0, and it reached a minimum value of 0.35 at the stoichiometric condition. At equivalence ratios higher than 7.0, the Lewis number was greater

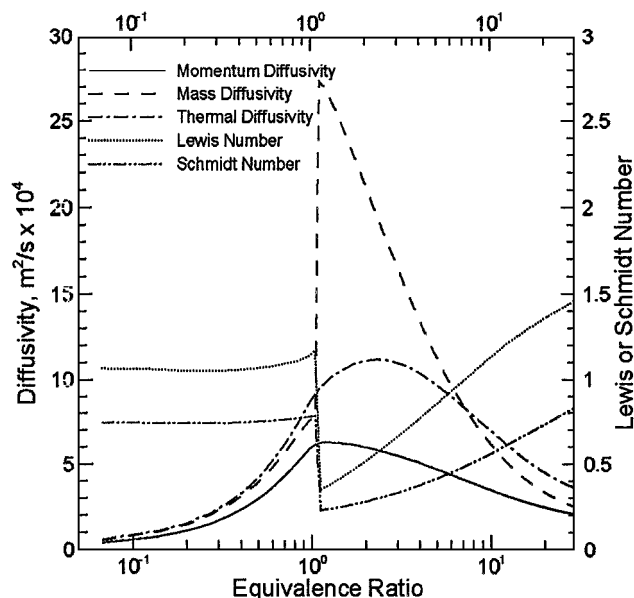


Fig. 2 Variation of transport properties with equivalence ratio in a hydrogen diffusion flame.

than 1.0. These variations in the Lewis number suggest that the difference between the two models developed for this study will be most significant in the fuel-rich side close to the flame. The Schmidt number, defined as the ratio of the momentum and mass diffusivities, varied with the equivalence ratio, and it reached a minimum value of about 0.2 at the stoichiometric condition.

Solution Procedure

The governing equations were integrated over a nonuniform staggered-grid system using the control-volume formulation.³⁰ The convection-diffusion terms in Eq. (11) were approximated using the hybrid differencing scheme.³¹ Harmonic averaging was used to evaluate transport properties at the interface of a control volume.³⁰ The resulting sets of pressure-velocity coupled algebraic equations were solved using a variant of the SIMPLE algorithm.³⁰ Variable grids were employed in the axial direction with increasing grid size downstream of the jet tube. Similarly, finer radial grids were used near the jet tube. The flow at the jet exit was fully developed because the jet tube was long compared with its diameter. The computational domain extended upstream of the jet exit to resolve the ambient flow entrainment and upstream diffusion. A constant pressure was specified away from the jet exit, in both the radial and axial directions. The axial diffusion at the exit boundary, placed sufficiently far downstream from the jet exit, was specified as zero. CFD results of the flowfield were processed to create the rainbow schlieren image using the numerical procedure outlined in the preceding section.

Results and Discussion

In this section we present detailed comparisons between computational and experimental results of mixing of a helium jet in air and a hydrogen jet diffusion flame. In each case, we compare 1) the rainbow schlieren images, 2) the distributions of the path-integrated data, and 3) the scalar field distributions to demonstrate the quantitative information gained by the RSD technique.

Helium Jet

The computational domain for the helium jet extended $5.5d$ in the radial direction and $25d$ in the axial direction. The upstream boundary was placed at a distance of $2d$ below the jet exit. A convergence check was performed using 35 radial and 96 axial or 35×96 , 69×96 , and 94×170 grids. Figure 3 shows the radial profiles of the helium mole fraction at $z/d = 13.5$ using different grids. Evidently, the solution was unaffected by the number of grids in the radial direction. Based on these results, the final calculations were done using the 94×170 grid. The grid size in the radial direction varied from 0.5 to 1.4 mm, and that in the axial direction was between 0.1

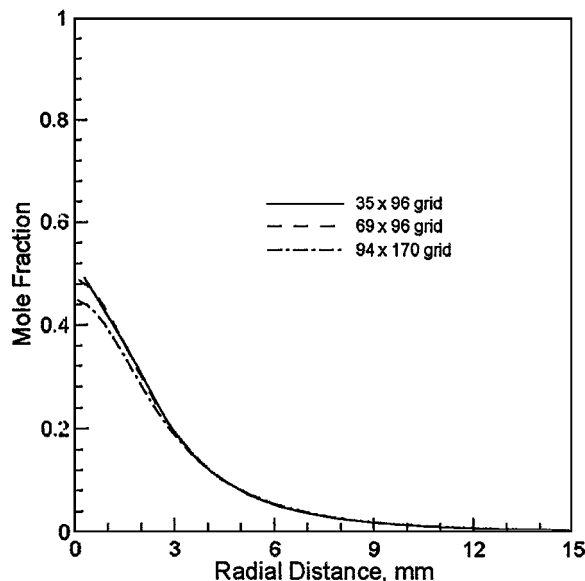


Fig. 3 Radial profiles of helium mole fraction at $z/d = 13.5$.

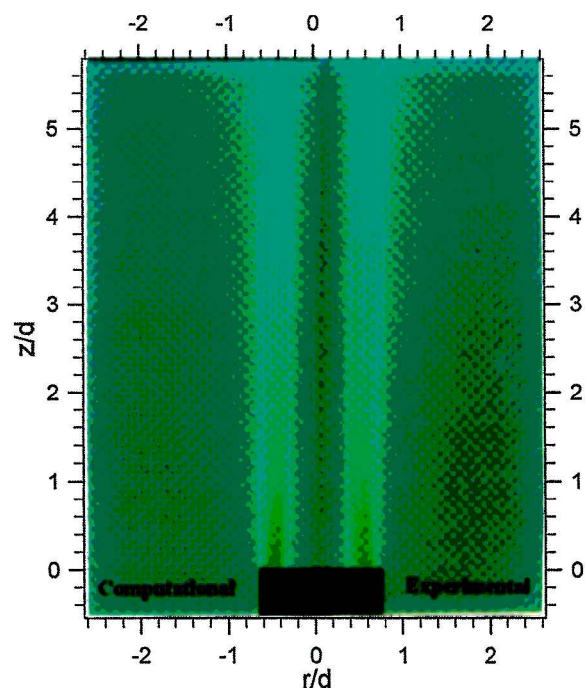


Fig. 4 Computed and experimental color schlieren images of the helium jet.

and 1.2 mm. The computational results were used to generate the schlieren image shown on the left-hand side in Fig. 4. The image on the right-hand side in Fig. 4 was obtained experimentally. The computational image in Fig. 4 was scaled with the experimental image having a limited field of view, and therefore, it depicts only a portion of the computational domain. The experimental image was processed to eliminate pixel-to-pixel variations in saturation and intensity caused by the schlieren apparatus. To be consistent with the computational image, the saturation and intensity in the experimental image were assigned a value of 1.0.

The color variations in Fig. 4 reveal the light ray deflections. Radially, far away from the jet centerline, we observe a uniform background color (or hue) corresponding to the undeflected rays. This color is also seen at the centerline where the transverse ray deflection is zero because of the flow symmetry. Figure 4 reveals that the color distributions in the experimental and computational images match visually. The largest color change occurred in the shear layer near the jet exit identified by a small yellow patch. The

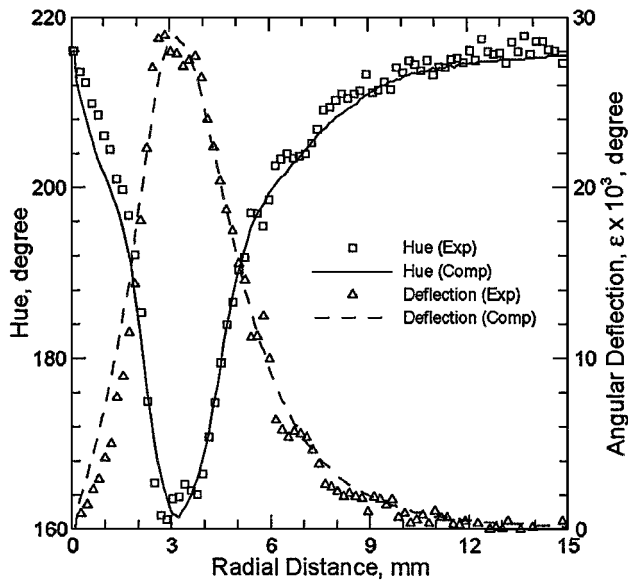


Fig. 5 Radial profiles of hue and angular deflections in the helium jet at $z/d = 1.0$.

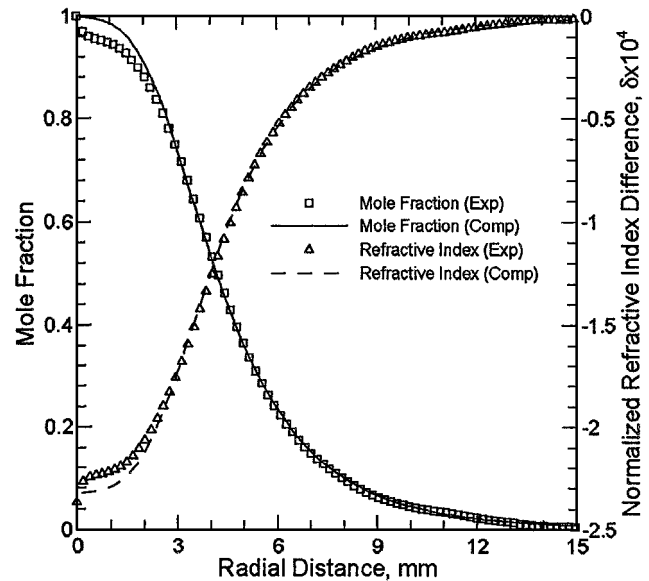


Fig. 7 Radial profiles of helium mole fraction and normalized refractive index difference in the helium jet at $z/d = 3.4$.

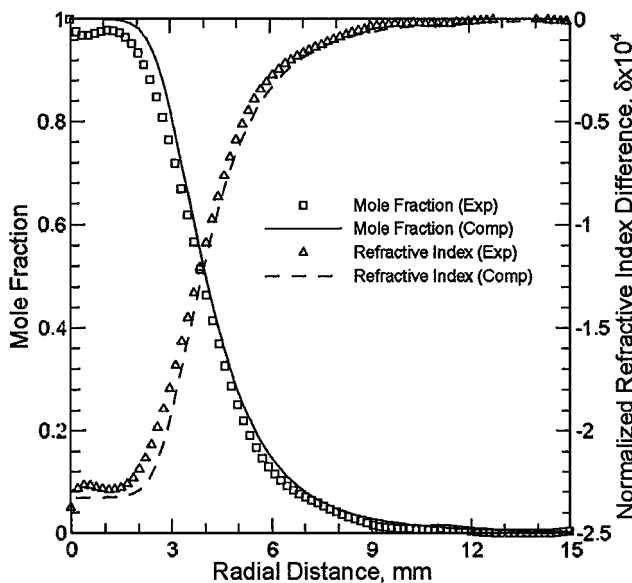


Fig. 6 Radial profiles of helium mole fraction and normalized refractive index difference in the helium jet at $z/d = 1.0$.

colors diffused downstream of the jet exit because of the mixing between the helium and air. A large portion of the jet center had similar colors, suggesting small angular deflections in those regions.

Although the experimental and computational schlieren images in Fig. 4 reveal similar features, a quantitative comparison is made in Fig. 5, which shows radial profiles of hue and angular deflection at $z/d = 1$. Because of the symmetry, the profiles in Fig. 5 are shown for only one side of the image. Also, the experimental results are shown for every alternate data point. Figure 5 reveals excellent agreement between measurements and computations. In the experiment, the hue reached a minimum value of 160 deg at $r = 3.0$ mm, where the angular deflection was the maximum. The experimental data and computations exhibit the schlieren boundary at $r = 15$ mm, where the angular deflections were zero. Overall, results indicate good agreement between measurements and computations.

In Figs. 6 and 7, we present quantitative comparisons of the refractive index and helium mole fraction distributions at $z/d = 1$ and 3.4. The computed results in Fig. 6 show that the normalized refractive index difference was minimum near the jet center, which agrees with the experimental data. The refractive index distributions from the experiment and computations agreed except for minor differences near the jet center. A similar trend was observed for the

helium mole fraction. Smaller gradients in the center region result in smaller angular deflections, which require high measurement resolution and sensitivity. The observed discrepancies are, therefore, attributed mainly to the measurement errors in the center region. The refractive index and helium mole fraction distributions at $z/d = 3.4$ are shown in Fig. 7. Once again an excellent agreement is reached between experimental data and computations, except within 2 mm from the jet center, where deviations of up to $\pm 2\%$ occur. From the visual and quantitative comparisons in Figs. 4–7, we conclude that the present CFD model accurately predicted mixing of the helium jet with air. The RSD technique was proven to be effective in validating the CFD results. We also found that higher measurement resolution and sensitivity are desired in regions of smaller gradients. Having reached these conclusions, we apply the RSD technique next to a more complex flowfield with chemical reactions.

Hydrogen Diffusion Flame

The diffusion flame in the experiment was obtained by injecting hydrogen into quiescent air from a 1.19-mm-i.d. jet tube of 0.42-mm wall thickness. The average jet exit velocity was 6.2 m/s, and the cold-flow Reynolds number at the jet exit was 70. The computations were done in a domain extending $20d$ in the radial direction and $45d$ in the axial direction. The upstream boundary was placed $10d$ below the jet exit. A nonuniform grid with 139 radial and 195 axial points was used for calculations with the two models. The spatial grid resolution in the radial direction varied from 0.07 to 0.60 mm, and that in the axial direction varied from 0.06 to 0.49 mm. The computed results from the two-zone diffusion model 2 were used to create the color schlieren image on the left-hand side of Fig. 8, scaled with the processed experimental image on the right-hand side. The two images in Fig. 8 have similar shapes, widths, and color distributions, although colors in the experimental images appear more diffuse. For example, the yellowish region in the computed image is larger and longer and has more striations than the image from the experiments. The flame tip in the present experiment was approximately at $z/d = 15$. However, the tip closing or the flame boundary cannot be detected from the schlieren image. The upstream diffusion is evident in both images, with the computational image showing a greater extent. This discrepancy arises possibly because the computations assumed an insulated jet tube. In the experiment, heat transfer to the tube wall lowers the temperature and, consequently, diffusivities inside the flame. The present models did not account for the thermal quenching by the tube wall. Overall, the computational trends agree with the experimental data, although visual comparison has its limitations. The schlieren image from model 1 is not shown because no significant differences between the two models were identified.

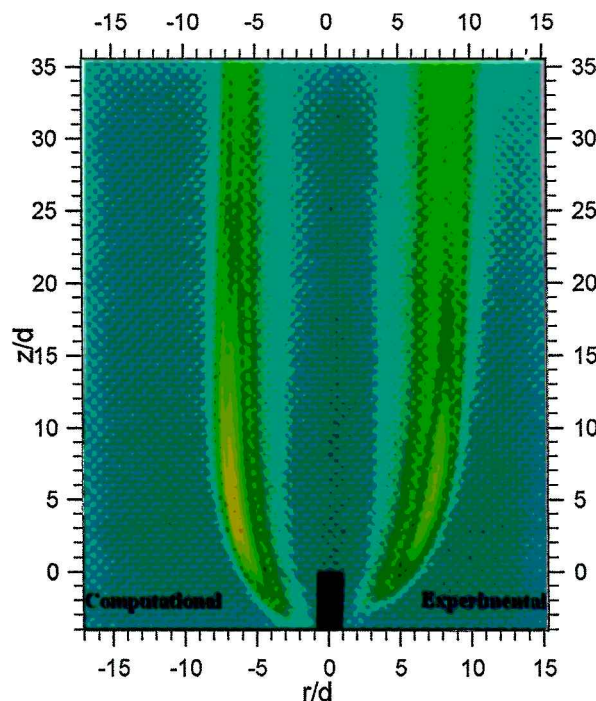


Fig. 8 Computed and experimental color schlieren images of the hydrogen diffusion flame.

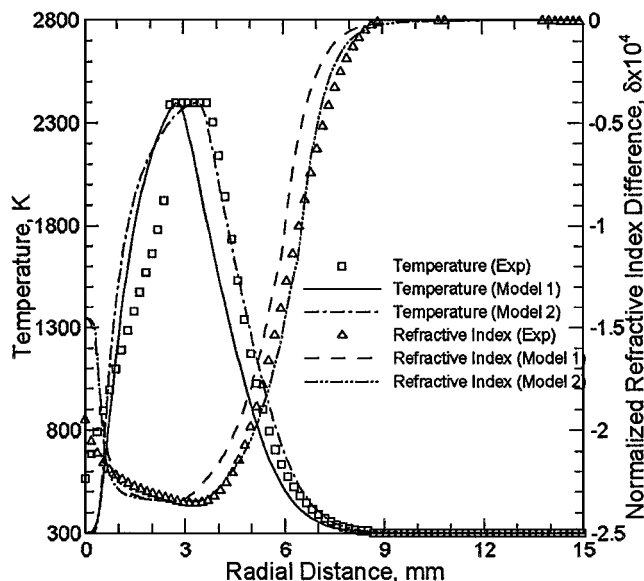


Fig. 10 Radial profiles of temperature and normalized refractive index difference in the hydrogen diffusion flame at $z/d = 0.76$.

dictions indicated the minimum refractive index, corresponding to the maximum temperature or the flame boundary, at $r = 3.3$ mm. The flame temperature of 2400 K agreed with the CARS measurements in the hydrogen diffusion flame.³² The measured temperature profile in Fig. 10 is flat at the 2400-K level, where the refractive index was less than or equal to its minimum value $-2.3e^{-4}$ at the stoichiometric condition. Note that the temperature was assigned the maximum value of 2400 K if the measured normalized refractive index difference was below $-2.3e^{-4}$.

A comparison of the two models in Fig. 10 shows that the location of the minimum refractive index from model 1 was 0.6 mm toward the center as compared with that from model 2. This shift represents the difference in the predicted flame location from the two models. The predicted flame width from model 1 was smaller than that from model 2 because the thermal diffusivity in model 1, used to represent the mixing inside the flame, was lower than the hydrogen mass diffusivity in model 2. The refractive index and temperature distributions in the fuel-lean region from the two models were separated by a constant radial distance. Evidently, the two models differed in predicting the flame location but concurred with each other outside the flame. Predictions from the two models were the same because the Lewis number was near unity in the fuel-lean region (see Fig. 2). The agreement reached between the experimental data and computations confirms that the fast-chemistry assumption is valid outside the flame. The primary difference between the two models was in the fuel-rich region close to the flame, where the Lewis number was far below unity. Although the predicted refractive index curves in this region agreed with the experimental data, the temperature distributions indicated substantial deviations. Evidently, the temperature is extremely sensitive to the refractive index difference in the fuel-rich region near the flame. Predictions from both models departed from the experimental data at the center. The measurements show a lower refractive index (or higher temperature) in the center compared with the model predictions. This difference is caused, in part, by preheating of the fuel because of the heat transfer from the jet tube wall. To explore this issue we examine next the refractive index and temperature distributions upstream of the jet exit at $z/d = -0.42$ in Fig. 11.

The experimental data in Fig. 11 identified the flame boundary at $r = 2.5$ mm, where the refractive index was the minimum and the temperature was the highest. The measured flame temperature of 2400 K was the same as that at $z/d = 0.76$. Contrary to the result at $z/d = 0.76$ in Fig. 10, the measured flame boundary in Fig. 11 was closer to the model 1 prediction. The measured refractive index difference and temperature distributions in the fuel-lean region also agreed with the model 1 predictions. Model 2 distributions in the fuel-lean region were similar to those from model 1 but shifted radially outward by approximately 1.0 mm or the difference in the

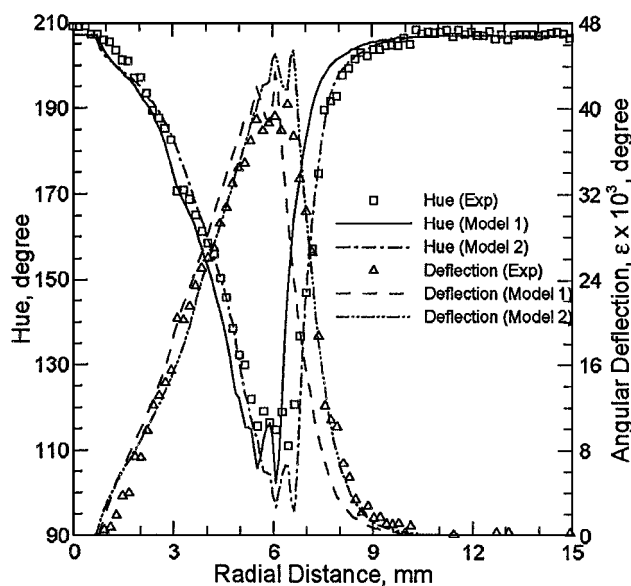


Fig. 9 Radial profiles of hue and angular deflections in the hydrogen diffusion flame at $z/d = 0.76$.

Next, in Fig. 9, we show radial profiles of hue and angular deflection at $z/d = 0.76$. The hue in Fig. 9 varied from a maximum of 210 deg in the background and center to a minimum of about 100 deg at $r = 6$ mm. The schlieren boundary was within $r = 11$ mm. Figure 9 reveals that both models predicted the hue distribution quite well, although model 2 indicated a closer agreement with the experimental data. The maximum angular deflection of 0.045 deg was at $r = 6$ mm. The results in Fig. 9 suggest that model 2 performed better than model 1; however, a quantitative distinction between the two models was not made.

Figure 10 compares the measured and predicted distributions of the normalized refractive index difference and temperature at $z/d = 0.76$. The relationship between the refractive index and temperature was established assuming the chemical equilibrium. Figure 10 shows an excellent agreement between the experimental data and computations using model 2. The main difference was in the center region up to $r = 0.5$ mm. The data and model 2 pre-

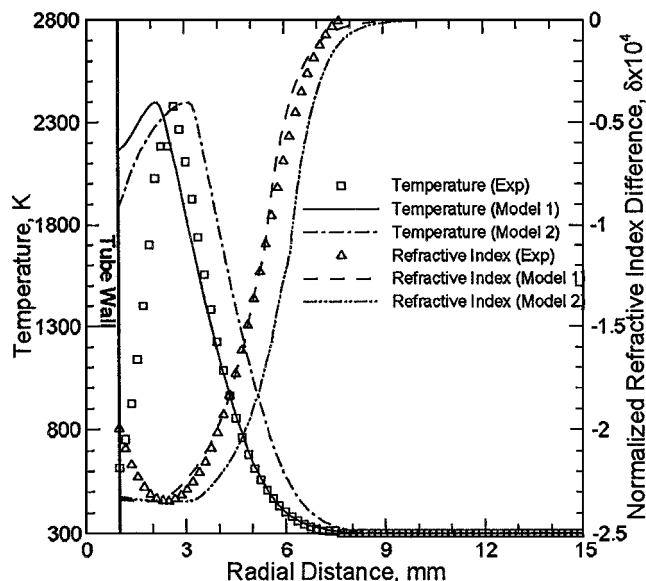


Fig. 11 Radial profiles of temperature and normalized refractive index difference in the hydrogen diffusion flame at $z/d = -0.42$.

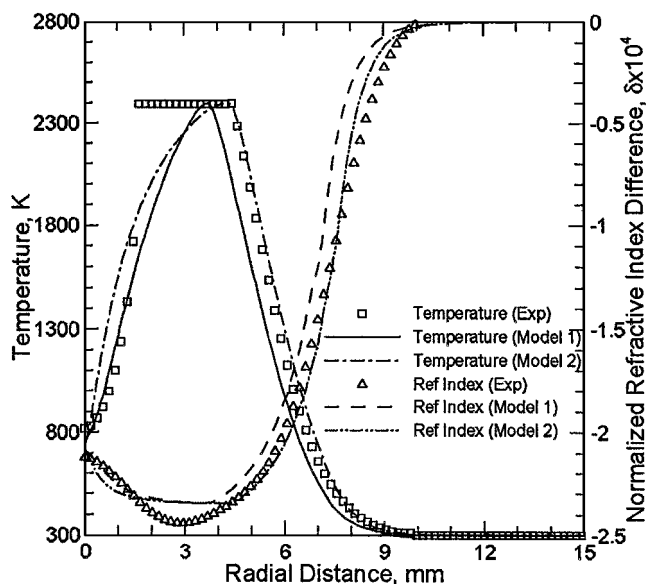


Fig. 12 Radial profiles of temperature and normalized refractive index difference in the hydrogen diffusion flame at $z/d = 3.5$.

predicted flame widths from the two models. These results confirm the earlier conclusion that the unity Lewis number and fast-reaction limit are adequate to simulate the fuel-lean region of the laminar hydrogen diffusion flame. Because the flame resided upstream of the jet exit, we conclude that the fully elliptic governing equations and an upstream computational domain are required for accurate flow predictions. In spite of the excellent agreement outside the flame, the model predictions differed from measurements inside the flame. Specifically, the measurements reveal a higher temperature gradient as compared with the predictions. The measured temperature near the tube wall was substantially lower than that predicted by the models. This result substantiates the role of heat transfer through the tube wall causing preheating of the fuel inside the jet tube and identifies the weakness of the present models in not accounting for the wall heat transfer. The close agreement reached between measurements and predictions from model 1 in Fig. 12 is explained as follows: The thermal quenching inside the flame decreased the temperature and, hence, the mass diffusivity that was not accounted for in model 2. Model 1 using the thermal diffusivity performed better by indirectly accounting for the decrease in the mass diffusivity.

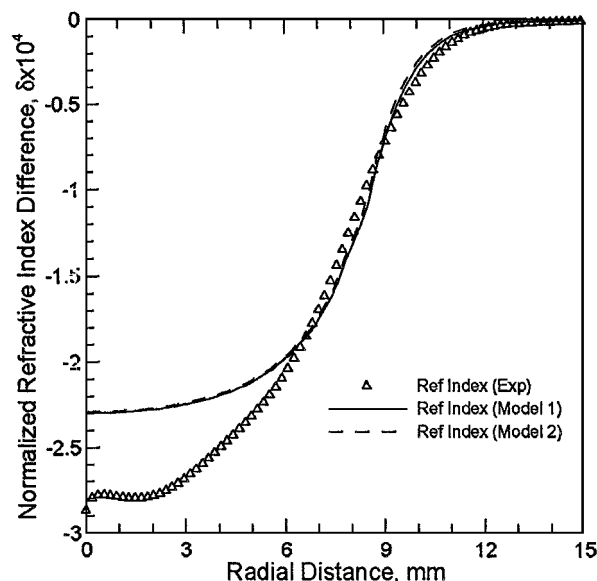


Fig. 13 Radial profiles of temperature and normalized refractive index difference in the hydrogen diffusion flame at $z/d = 20.0$.

The results presented have shown that both models are valid outside the flame and that the hydrogen mass diffusivity in model 2 correctly represents mixing near the jet exit. Next we compare measurements and predictions midway in the flame ($z/d = 3.5$) and downstream of the flame ($z/d = 20.0$). The normalized refractive index difference and temperature distributions from experiment and predictions at $z/d = 3.5$ are compared in Fig. 12. The predicted flame boundaries using models 1 and 2 were, respectively, at $r = 3.0$ and 4.0 mm. Predictions using model 2 agreed with measurements beyond the flame boundary. Model 1 predictions outside the flame were similar but shifted radially inward by approximately 1 mm because of the difference in the predicted flame locations from the two models. Predictions using either of the two models deviated from measurements in the fuel-rich region near the flame. The measured refractive index difference surpassed its minimum value in the region where the temperature profile is flat at the 2400-K level. The predictions in this region show a nearly constant refractive index. This discrepancy between measurements and predictions is attributed to 1) the differential/preferential diffusion effects not accounted for in the models and/or 2) the accuracy of the schlieren apparatus, which suffers in regions of small gradients, as already discussed.

Finally, we compare the predicted and measured distributions of the refractive index difference in the heated jet region at $z/d = 20$ in Fig. 13. Nearly identical predictions from the two models signify validity of the unity Lewis number. The model predictions agreed with measurements only in the outer regions with $r > 6$ mm. The measured refractive index in the center region exceeded its minimum value by as much as 20%. Thus, the temperature at this axial location was not resolved quantitatively for $r < 6$ mm. These results substantiate that higher sensitivity and resolution of the schlieren apparatus are necessary in regions of small gradients.

Conclusions

This work has shown that RSD is useful to validate CFD models of reacting and nonreacting steady flows in axisymmetric systems. Specifically, the following conclusions are drawn:

- 1) A steady, laminar helium jet in ambient air was accurately modeled using the ideal gas law and Wilke's mixture-averaged formula to relate the physical and transport properties to the helium mass fraction.
- 2) The unity Lewis number and fast-chemistry assumptions are valid in the air side of the reaction zone of a hydrogen diffusion flame.
- 3) The upstream diffusion and preheating of the fuel in the jet tube should be considered to accurately predict the laminar gas jet diffusion flames.

4) The mass diffusivity of hydrogen adequately represents the mixing inside the diffusion flame near the jet exit. However, the differential and/or preferential diffusion effects in the fuel side of the reaction zone require consideration of the nonunity Lewis number.

5) The calculations identified regions of small gradients where high resolution and sensitivity of the schlieren measurements were necessary.

Acknowledgments

This research was supported by NASA Microgravity Research Division Grant NAG 3-1594. We wish to thank DeVon Griffin and Paul Greenberg at NASA Lewis Research Center for providing helpful comments on the manuscript.

References

- ¹Marvin, J. G., "Perspectives on Computational Fluid Dynamics Validation," *AIAA Journal*, Vol. 33, No. 10, 1995, pp. 1778-1787.
- ²Taylor, A. M. K. P., *Instrumentation for Flows with Combustion*, Academic, New York, 1993, pp. 53-107.
- ³Goldstein, R. J., and Kuehn, T. H., "Optical Systems for Flow Measurement: Shadowgraph, Schlieren, and Interferometric Techniques," *Fluid Mechanics Measurements*, edited by R. J. Goldstein, Taylor and Francis, Washington, DC, 1996, pp. 451-502.
- ⁴Yates, L. A., "Images Constructed from Computed Flow Fields," NASA CR-194397, Jan. 1992.
- ⁵Yates, L. A., "Constructed Interferograms, Schlieren, and Shadowgraph: A Users Manual," NASA CR-194530, Oct. 1993.
- ⁶Schopf, W., Patterson, J. C., and Brooker, A. M. H., "Evaluation of the Shadowgraph Method for Convective Flow in a Side-Heated Cavity," *Experiments in Fluids*, Vol. 21, No. 5, 1996, pp. 331-340.
- ⁷Greenberg, P. S., Klimek, R. B., and Buchele, D. R., "Quantitative Rainbow Schlieren Deflectometry," *Applied Optics*, Vol. 34, No. 19, 1995, pp. 3810-3822.
- ⁸Agrawal, A. K., Butuk, N. K., Gollahalli, S. R., and Griffin, D., "Three-Dimensional Rainbow Schlieren Tomography of a Temperature Field in Gas Flows," *Applied Optics*, Vol. 37, No. 3, 1998, pp. 479-485.
- ⁹Al-Ammar, K., Agrawal, A. K., Gollahalli, S. R., and Griffin, D., "Application of Rainbow Schlieren Deflectometry for Concentration Measurements in an Axisymmetric Helium Jet," *Experiments in Fluids*, Vol. 25, No. 2, 1998, pp. 89-95.
- ¹⁰Agrawal, A. K., Gollahalli, S. R., and Griffin, D. W., "Study of Buoyancy Effects in Diffusion Flames Using Rainbow Schlieren Deflectometry," *Proceedings of the 4th International Microgravity Combustion Workshop*, NASA CP-10194, 1997, pp. 117-122.
- ¹¹Weinberg, F. J., *Optics of Flames*, Butterworths, London, 1963, pp. 23-39.
- ¹²Rubinstein, R., and Greenberg, P. S., "Rapid Inversion of Angular Deflection Data for Certain Axisymmetric Refractive Index Distribution," *Applied Optics*, Vol. 33, No. 7, 1994, pp. 1141-1144.
- ¹³Vasil'ev, L. A., *Schlieren Methods*, Israel Program for Scientific Translation, New York, 1971, pp. 171-205.
- ¹⁴Press, W. H., Teukolsky, S. A., Vetterling, W. T., and Flannery, B. P., *Numerical Recipes in Fortran*, Cambridge Univ. Press, New York, 1992, pp. 116-118.
- ¹⁵Kyle, D. M., "The Instability and Breakdown of a Round Variable-Density Jet," Ph.D. Thesis, Mechanical Engineering, Yale Univ., New Haven, CT, Dec. 1991.
- ¹⁶Bird, R. B., Stewart, W. E., and Lightfoot, E. N., *Transport Phenomena*, Wiley, New York, 1960, p. 571.
- ¹⁷Bilger, R. W., "The Structure of Diffusion Flames," *Combustion Science and Technology*, Vol. 13, 1976, pp. 155-170.
- ¹⁸Gore, J. P., Jeng, S.-M., and Faeth, G. M., "Spectral and Total Radiation Properties of Hydrogen/Air Diffusion Flames," *Journal of Heat Transfer*, Vol. 109, 1987, pp. 165-171.
- ¹⁹Faeth, G. M., and Samuelson, G. S., "Fast Reaction Non Premixed Combustion," *Progress in Energy and Combustion Science*, Vol. 12, 1986, pp. 305-372.
- ²⁰Katta, V. R., Goss, L. P., and Roquemore, W. M., "Effects of Nonunity Lewis Number and Finite Rate Kinetics on the Dynamics of a Hydrogen-Air Jet Diffusion Flame," *Combustion and Flame*, Vol. 96, No. 1-2, 1994, pp. 60-74.
- ²¹Katta, V. R., Goss, L. P., and Roquemore, W. M., "Numerical Investigations of Transitional H₂/N₂ Jet Diffusion Flames," *AIAA Journal*, Vol. 32, No. 1, 1994, pp. 84-94.
- ²²Grinstein, F. F., and Kailasanath, K., "Three-Dimensional Numerical Simulations of Unsteady Reactive Square Jets," *Combustion and Flame*, Vol. 100, No. 1-2, 1995, pp. 2-10.
- ²³Kee, R. J., Rupley, F. M., and Miller, J. A., "Chemkin-II: A Fortran Chemical Kinetics Package for the Analysis of Gas Phase Chemical Kinetics," Sandia National Labs., SAND89-809B-UC-706, Albuquerque, NM, Aug. 1993.
- ²⁴Smith, L. L., Dibble, R. W., Talbot, L., Barlow, R. S., and Carter, C. D., "Laser Raman Scattering Measurements of Differential Molecular Diffusion in Turbulent Nonpremixed Jet Flames of H₂/CO₂ Fuel," *Combustion and Flame*, Vol. 100, No. 1-2, 1995, pp. 153-160.
- ²⁵Takagi, T., Xu, Z., and Komiya, M., "Preferential Diffusion Effects on the Temperature in Usual and Inverse Diffusion Flames," *Combustion and Flame*, Vol. 106, No. 3, 1996, pp. 252-260.
- ²⁶Bilger, R. W., "Molecular Transport Effects in Turbulent Diffusion Flames at Moderate Reynolds Number," *AIAA Journal*, Vol. 20, No. 7, 1982, pp. 962-970.
- ²⁷Chung, S. H., and Law, C. K., "Burke-Schumann Flame with Streamwise and Preferential Diffusion," *Combustion Science and Technology*, Vol. 37, 1984, pp. 21-46.
- ²⁸Takagi, T., and Xu, Z., "Numerical Analysis of Laminar Diffusion Flames—Effects of Preferential Diffusion of Heat and Species," *Combustion and Flame*, Vol. 96, No. 1-2, 1994, pp. 50-59.
- ²⁹Kee, R. J., Dixon-Lewis, G., Warnatz, J., Coltrin, M. E., and Miller, J. A., "A Fortran Computer Code Package for the Evaluation of Gas Phase Multicomponent Transport Properties," Sandia National Labs., SAND86-8246-UC401, Albuquerque, NM, May 1993.
- ³⁰Patankar, S. V., *Numerical Heat Transfer and Fluid Flow*, McGraw-Hill, Washington, DC, 1980, pp. 82-130.
- ³¹Spalding, D. B., "A Novel Finite-Difference Formulation for Differential Expressions Involving Both First and Second Derivatives," *International Journal for Numerical Methods in Engineering*, Vol. 4, 1972, p. 551.
- ³²Hancock, R. D., Schauer, F. R., Lucht, R. P., Katta, V. R., and Hsu, K. Y., "Thermal Diffusion Effects and Flame-Vortex Interactions in Hydrogen Jet Diffusion Flames," *Twenty-Sixth Symposium (International) on Combustion*, Combustion Inst., Pittsburgh, PA, 1996, pp. 1087-1093.

K. Kailasanath
Associate Editor